Geophysical Prospecting

EAGE EUROPEAN ASSOCIATION OF GEOSCIENTISTS & ENGINEERS

Geophysical Prospecting, 2015 doi: 10.1111/1365-2478.12287

Theoretical analysis of non-geometric PS-waves recorded at the water bottom interface

Nihed Allouche*,† and Guy Drijkoningen

Department of Geotechnology, Delft University of Technology, 2600 GA Delft, The Netherlands

Received December 2014, revision accepted April 2015

ABSTRACT

When a seismic source is placed in the water at a height less than a wavelength from the water–solid interface, a prominent S-wave arrival can be observed. It travels kinematically as if it was excited at the projection point of the source on the interface. This non-geometric S-wave has been investigated before, mainly for a free-surface configuration. However, as was shown in a field experiment, the non-geometric S-wave can also be excited at a fluid–solid configuration if the S-wave speed in the solid is less than the sound speed in the water. The amplitude of this wave exponentially decreases when the source is moved away from the interface revealing its evanescent character in the fluid. In the solid, this particular converted mode is propagating as an ordinary S-wave and can be transmitted and reflected as such. There is a specific region of horizontal slownesses where this non-geometric wave exists, depending on the ratio of the S-wave velocity and the sound speed of water. Only for ratios smaller than 1, this wave appears. Lower ratios result in a wider region of appearance. Due to this property, this particular P-S converted mode can be identified and filtered from other events in the Radon domain.

Key words: Non-geometric waves, S-waves, Radon transform.

1 INTRODUCTION

Non-geometric S-waves are excited when the dominant wavelength of a point source exceeds the distance between the source and a plane interface separating two media with different elastic properties (Hron and Mikhailenko 1981). The excited S-waves appear to be originating from the projection point of the source on the interface. Because the existence of such a wave mode is not predicted by ray-based methods, their kinematic behaviour is considered to be non-geometric. The existence of this type of arrivals was predicted in theory by Brekhovskikh (1960) and categorized along with the head waves as lateral waves. Hron and Mikhailenko (1980) were the first to report the existence of a specific type of non-geometric S-wave in their synthetic seismogram. This arrival, referred to in seismology as S*, was generated by a P-wave source buried close to the free surface. In the past decades, other non-geometric S-modes, including the SH*-arrival (Daley and Hron 1988) and more recently the $\bar{P}S$ phase (Roth and Holliger 2000), have been identified in synthetic and real data.

The S*-arrivals are physically interpreted as evanescent P-waves tunnelling to the free-surface interface where they convert to propagating shear mode (Daley and Hron 1983). Evanescent waves are often neglected because of their exponentially decaying amplitude as a function of depth. However, when the source is moved closer to the interface, the conversion of the tunnelling P-waves to propagating S-mode becomes more significant (Gutowski *et al.* 1984). In this way, their detectability in synthetic seismograms increases.

Recently, field data evidence of non-geometric PS-converted waves has renewed our interest in this particular type of arrivals. Unlike S*, these waves were observed in a data

*E-mail: nallouche@slb.com
†Present address: Schlumberger Gould Research, High Cross, Madingley Road, Cambridge CB3 0EL, UK.

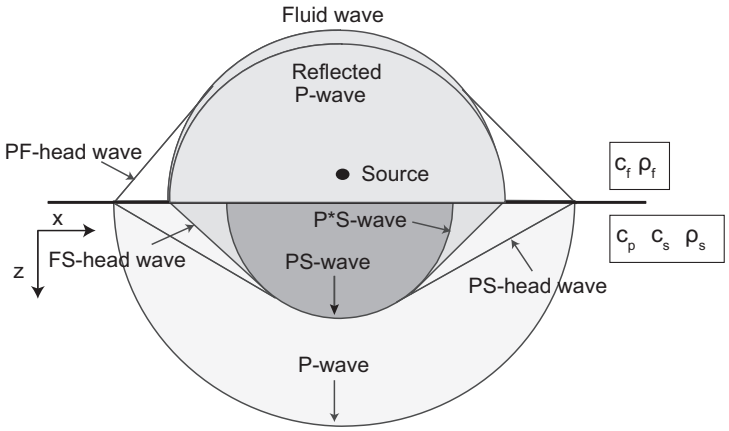

Figure 1 Schematic of the wavefield generated by a source located in a fluid half-space overlying a solid half-space.

set acquired in a shallow-water environment (Allouche *et al.* 2011). They were generated by a source with a low-frequency content towed in the water and recorded by 3-C geophones and hydrophones placed on the water bottom. Due to the low apparent velocity of these waves and the linear horizontal polarization, the hyperbolic shaped arrivals were interpreted as S-wave reflections. The modelling study in the same paper revealed that these S-waves are not travelling according to Snell's law and were consequently classified as non-geometric.

In this paper, we show that the recently discovered non-geometric PS-wave features the same properties as S*. We verify the existence of this specific mode in a fluid–solid configuration by deriving and computing the transmitted wavefield in the solid. Using the Cagniard–de Hoop technique, the main properties of the PS-conversion in the near field are studied and their relevance to shallow marine seismics is discussed. Finally, we propose a method to separate the modes converted at the water bottom from the data using the Radon transform.

2 TRANSMITTED WAVEFIELD IN A FLUID–SOLID CONFIGURATION

2.1 Theory of non-geometric PS-conversion

To understand the nature of the non-geometric PS-waves, we derive the transmitted wavefield for the fluid–solid configuration shown in Fig. 1. The source is located at height z_s in the upper half-space ($z < 0$) consisting of an ideal fluid, and the receivers are buried in the homogeneous, isotropic, and elastic solid ($z > 0$). The generated pressure field $P(x, z, t)$, propagating in the fluid with a speed c_f, satisfies the inhomogeneous wave equation

$$\nabla^2 P - \frac{1}{c_f^2}\frac{\partial^2 P}{\partial t^2} = -\delta(x, z)S(t), \tag{1}$$

where $S(t)$ denotes the source signature. When we consider a Cartesian coordinate system and assume a line source along the y-direction, a well-known solution of this equation can be written in terms of Weyl's integral, representing a superposition of plane waves (Aki and Richards 2002)

$$\begin{aligned} P_i(x, z, t) &= \frac{1}{4\pi r}S(t - r/c_f) \\ &= \frac{1}{(2\pi)^2}\int\!\!\int_{-\infty}^{\infty}\frac{S(\omega)}{2jq_f}\mathrm{e}^{j\omega(t-px-q_f|z-z_s|)}dpd\omega, \end{aligned} \tag{2}$$

in which $r = \sqrt{x^2 + z^2}$ and where $S(\omega)$ is the source spectrum, p is the horizontal slowness, and ω is the angular frequency. The right-hand side of equation (2) is the time-domain solution of the inhomogeneous wave equation for a monopole point source, whereas the left-hand side represents the same solution but obtained in the frequency-wavenumber domain. These two solutions are equal after applying an inverse Fourier transform to the frequency-wavenumber solution and evaluating the integral over the vertical slowness using Cauchy's residue theorem (Aki and Richards 2002). To satisfy the radiation condition, we define the vertical slowness in the fluid as $q_f = \sqrt{1/c_f^2 - p^2}$ with $\mathrm{Im}(q_f) < 0$.

In the solid, the particle velocity $v(x, z, t)$ is governed by the elastic wave equation:

$$(\lambda + \mu)\nabla(\nabla \cdot v) - \mu\nabla \times \nabla \times v - \rho_s\frac{\partial^2 v}{\partial t^2} = 0, \tag{3}$$

where λ and μ are the Lamé parameters and ρ_s is the density in the solid. The particle velocity can be decomposed into rotation-free P-wave and divergence-free S-wave contributions:

$$v(x, z, t) = v_p(x, z, t) + v_s(x, z, t). \tag{4}$$

Similarly to the pressure in the fluid, these contributions are expressed in terms of plane-wave superposition

$$v_x(x,z,t) = \frac{1}{(2\pi)^2}\iint_{-\infty}^{\infty}\frac{1}{2jq_f}\Big[A_x^p e^{j\omega(t-px-q_pz+q_fz_s)} + A_x^s e^{j\omega(t-px-q_sz+q_fz_s)}\Big]dpd\omega,$$
$$v_z(x,z,t) = \frac{1}{(2\pi)^2}\iint_{-\infty}^{\infty}\frac{1}{2jq_f}\Big[A_z^p e^{j\omega(t-px-q_pz+q_fz_s)} + A_z^s e^{j\omega(t-px-q_sz+q_fz_s)}\Big]dpd\omega \quad (5)$$

where v_x and v_z are the particle velocity components in the x- and z-direction, respectively. The vertical slownesses q_p and q_s, associated with the P- and S-waves, satisfy the radiation condition such that

$$q_p = \sqrt{1/c_p^2 - p^2} \quad \text{with} \quad \mathrm{Im}(q_p) < 0, \quad (6)$$

$$q_s = \sqrt{1/c_s^2 - p^2} \quad \text{with} \quad \mathrm{Im}(q_s) < 0. \quad (7)$$

The amplitude factors of the transmitted P- and S-waves in the x-direction, A_x^p and A_x^s, and in the z-direction, A_z^p and A_z^s, are related to the amplitude of the source spectrum $S(\omega)$ according to

$$A_x^p = \frac{p}{\rho_f}S(\omega)T_p, \quad A_x^s = \frac{q_s}{\rho_f}S(\omega)T_s,$$
$$A_z^p = \frac{q_p}{\rho_f}S(\omega)T_p, \quad A_z^s = \frac{-p}{\rho_f}S(\omega)T_s, \quad (8)$$

where T_p is the transmission coefficient and T_s is the conversion coefficient. These coefficients are derived by satisfying the boundary conditions associated with a fluid–solid interface. Writing the coefficients as particle velocity ratios and in similar form as de Hoop and van der Hijden (1983) gives

$$T_p = (\rho_f/\rho_s)(1/2c_s^2 - p^2)/c_s^2\Delta_{SCH}, \quad (9)$$

$$T_s = -(\rho_f/\rho_s)pq_p/c_s^2\Delta_{SCH}, \quad (10)$$

with

$$\Delta_{SCH} = \rho_f q_p/4c_s^4\rho_s q_f + (p^2 - 1/2c_s^2)^2 + p^2 q_p q_s, \quad (11)$$

a term known as the Scholte-wave denominator and is associated with surface waves propagating along the fluid–solid interface (de Hoop and van der Hijden 1983). Substituting the expressions found for the amplitude factors in equation (5) results in

$$v_x(x,z,t) = \frac{1}{(2\pi)^2}\iint_{-\infty}^{\infty}\frac{S(\omega)}{2jq_f\rho_f}\Big[pT_p e^{j\omega(t-px-q_pz+q_fz_s)} + q_sT_s e^{j\omega(t-px-q_sz+q_fz_s)}\Big]dpd\omega,$$
$$v_z(x,z,t) = \frac{1}{(2\pi)^2}\iint_{-\infty}^{\infty}\frac{S(\omega)}{2jq_f\rho_f}\Big[q_pT_p e^{j\omega(t-px-q_pz+q_fz_s)} - pT_s e^{j\omega(t-px-q_sz+q_fz_s)}\Big]dpd\omega. \quad (12)$$

The total wavefield in the solid for a given frequency, composed of the transmitted P-wave and the converted S-wave, is obtained by integrating over the horizontal slowness p. The amplitude contribution to the PS-wave is determined by the conversion coefficient T_s, and their propagation is dependent on the vertical slownesses q_f and q_s. From the definition of these slownesses, it can be deduced that, when $c_s < c_f$, the vertical slowness associated with the pressure wave in the fluid, i.e., q_f, becomes imaginary for p-values exceeding $1/c_f$, whereas q_s, the vertical slowness related to the S-mode in the solid is still real in the range $1/c_f < p < 1/c_s$. In this particular case, the incident fluid wave with an amplitude decaying exponentially ($\sim e^{-\omega\sqrt{p^2-1/c_f^2}|z_s|}$) with depth is converted at the interface to a propagating S-mode giving rise to the non-geometric PS-wave (P*S). However, if $c_s > c_f$, the converted S-wave becomes imaginary for p-values larger than $1/c_s$, whereas the incident fluid wave is real in the p-value range $1/c_s < p < 1/c_f$. In this case, the S-wave is propagating only along the interface giving rise to the FS-head wave.

2.2 Synthetic example

To illustrate the difference between the geometric and non-geometric PS-conversions at the fluid–solid interface, we adopted two simple models consisting of a fluid half-space with $c_f = 1500$ m/s and $\rho_f = 1000$ kg/m^3 overlying an elastic layer with seismic properties representative of: (i) a slow formation with $c_p = 1650$ m/s, $c_s = 200$ m/s, and $\rho_s = 1200$ kg/m^3 and (ii) a fast formation with $c_p = 4500$ m/s, $c_s = 2100$ m/s, and $\rho_s = 2500$ kg/m^3. We also make a distinction between two types of conversions. One conversion occurs due to a source placed at height $h = 2\lambda$, and the second occurs due to a source placed at height $h = \lambda/8$ with respect to the interface, with λ being the dominant wavelength of the source. Figure 2 shows the transmitted responses computed using the reflectivity method (Fuchs and Müller 1971; Schmidt 1988) for receivers located 50 m below the fluid–solid interface.

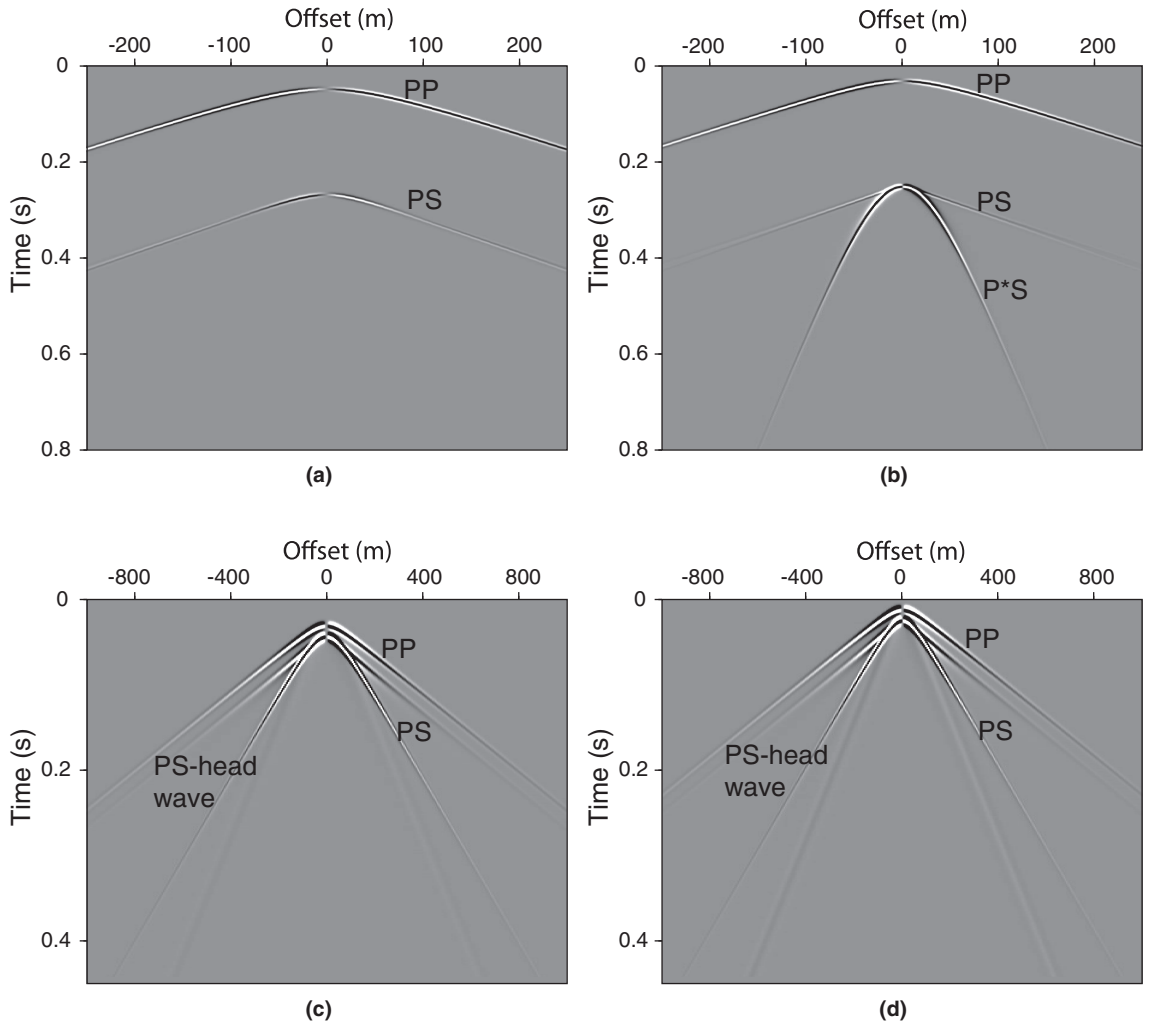

Figure 2 The horizontal particle velocity of the transmitted wavefields for: the soft formation model with the source located at height $h = 2\lambda$ (a) and $h = \lambda/8$ (b) above the interface and the stiff formation model with the source located at height $h = 2\lambda$ (c) and $h = \lambda/8$ (d) above the interface.

For the soft formation, the transmitted wavefield is composed of two events, namely, the transmitted P-wave and the converted S-wave. However, when the source is situated closer to the interface, a third distinctive event with a lower dominant frequency appears (see Fig. 2(a)). The low apparent velocity is indicative of this event identified as the non-geometric PS-wave (P*S). The difference between the two cases for the stiff solid is less visible, as shown in Fig. 2(b). In both cases, the response consists of the transmitted P-wave, the converted S-wave, and the PS-head wave.

2.3 Mapping the response in the linear Radon domain

As explained in the theory, the non-geometric arrivals are confined to a specific range of horizontal slownesses p between $1/c_f$ and $1/c_s$. A convenient way to illustrate this is to map the wavefield into the linear Radon domain (Deans, 1983) by merely summing the traces along lines with constant p according to

$$\tilde{v}(p, \Gamma) = \int_{-\infty}^{+\infty} v(x, \Gamma + px)dx, \tag{13}$$

where Γ is the intercept time defined as $\Gamma = t - px$. Because the horizontal slowness can also be defined as $p = \Delta t/\Delta x$, the transformed data can be interpreted as a summation of all the dip components present in the response. The steepest part of the slowest event, the asymptote of its hyperbola, is the maximum p-value at which the data are mapped in the (Γ, p) domain.

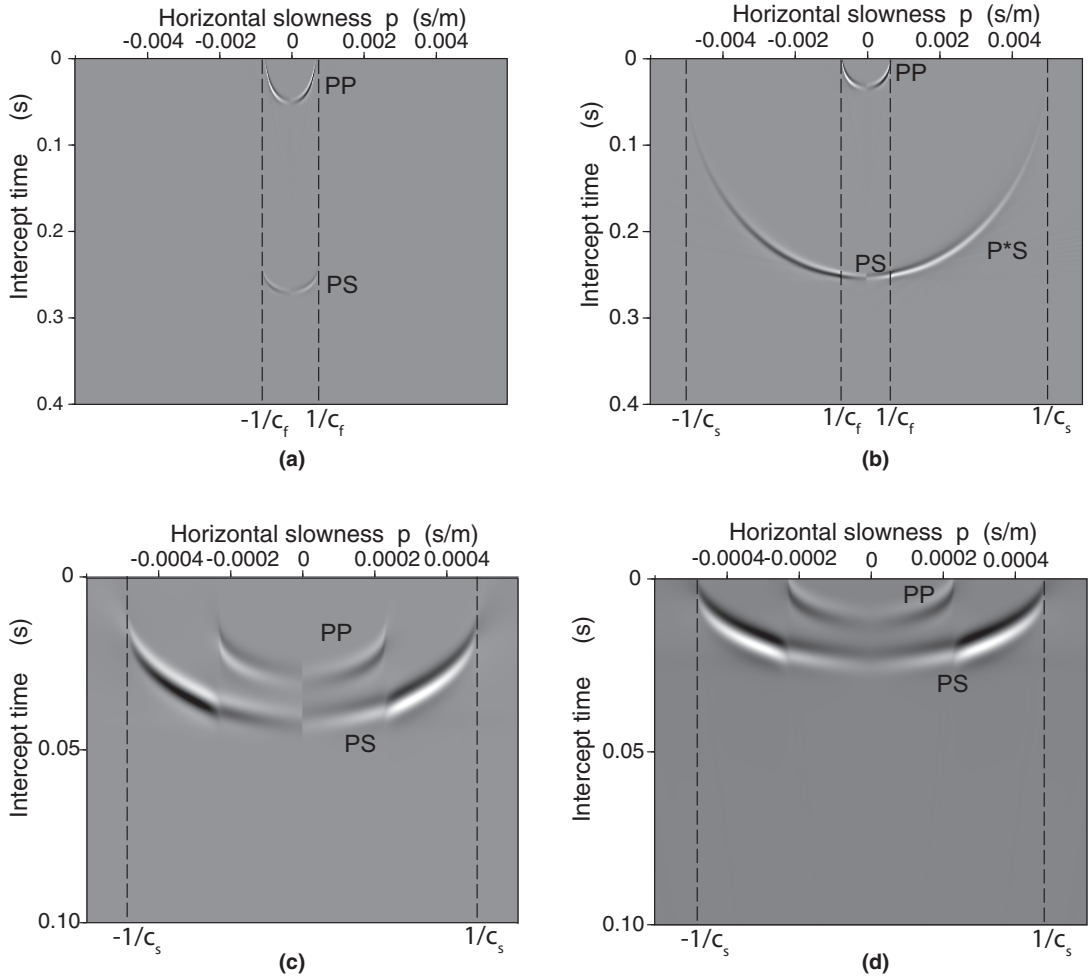

Figure 3 The horizontal particle velocity of the transmitted wavefield mapped in the linear Radon domain: the soft formation model with the source located at height $h = 2\lambda$ (a) and $h = \lambda/8$ above the interface (b) and the stiff formation model with the source located at height $h = 2\lambda$ (c) and $h = \lambda/8$ (d) above the interface. The dashed lines denote the maximum p-value of the geometric ($1/c_f$) and non-geometric waves ($1/c_s$).

For the soft formation example, with $h = 2\lambda$, the maximum p-value corresponds to the asymptote of the converted wave, which is equal to the inverse speed of the fluid wave as demonstrated in Fig. 3(a). However, if the source is placed at $h = \lambda/8$ and the non-geometric PS-wave is excited, it can be observed that the maximum p-value in this case becomes the inverse of the S-wave velocity. The non-geometric PS-wave is stacked along slopes ranging between $[-1/c_s, -1/c_f]$ and $[1/c_f, 1/c_s]$ and is not overlapping with the transmitted P-wave, making it easier to separate in this domain.

No notable differences, caused by changing the source height, are observed in the Radon-transformed responses of the stiff formation (compare Fig. 3(c) and 3(d)), confirming the fact that non-geometric PS-waves are not excited in this case.

3 PROPERTIES OF THE NON-GEOMETRIC PS-WAVE USING THE CAGNIARD–DE HOOP METHOD

Non-geometric arrivals have specific properties that distinguish them from other types of events: (i) they travel kinematically as if they were excited at the projection point of the source on the interface; (ii) their amplitudes exponentially decrease when the source is moved away from the interface, revealing their evanescent character in water; and (iii) they are confined to a specific region of horizontal slownesses. These properties are discussed in the literature mainly with reference to S*. In this section, we verify whether the identified non-geometric PS-mode, associated with a fluid–solid configuration, features the same properties. The Cagniard–de Hoop

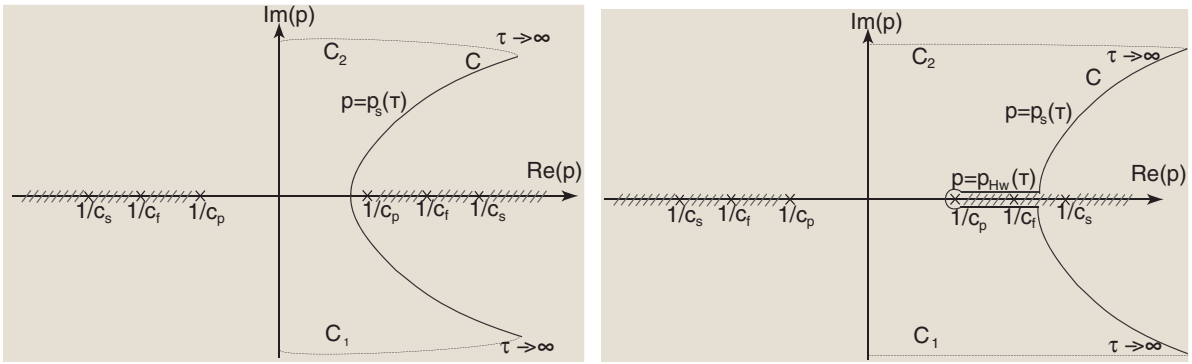

Figure 4 The modified integration path and the singularities $1/c_p$,$1/c_f$ and $1/c_s$ plotted in the complex p-plane. (a) The Cagniard path for receiver distance where no head waves are generated. (b) The extension in the integration path for receivers where head waves can occur.

method is suitable for this purpose because it provides an exact solution for the PS-converted wave, expressed explicitly in the space–time domain. This is done by modifying the integration path along p into a form that can be recognized as the impulse response or Green's function. The basics about this method are treated by several authors (de Hoop and van der Hijden 1983; Drijkoningen and Chapman 1988; Chapman 2004) and will not be discussed with many details in this paper.

We start by omitting the factor $S(\omega)$, associated with the source, from equation (12) and introduce it later to the time-domain expression by convolution. The PS-response in the space–frequency domain is then

$$\{\hat{v}_x^s(x,z,\omega),\hat{v}_z^s(x,z,\omega)\} = \frac{j}{2\pi}\int_{-\infty}^{\infty}\{C_x(p),C_z(p)\}T_s e^{-j\omega(px+q_s z-q_f z_s)}dp, \quad (14)$$

where $\{C_x(p),C_z(p)\}=\{-q_s/2q_f\rho_f,\, p/2q_f\rho_f\}$. The p-contour of integration can be distorted from the real axis to the Cagniard contour by solving for $\mathrm{Im}(\tau)=0$ where $\tau = px+q_s z-q_f z_s$.

Since function τ is quartic for p, the square roots are sought numerically. We are considering $c_s<c_f<c_p$, the case in which the non-geometric PS-waves are excited. Fig. 4(a) schematically shows the Cagniard path along which function τ is evaluated. It is possible that p_s, the p-value corresponding to the transmitted S-wave, crosses the branch cuts $1/c_p$ and $1/c_f$ given rise to head waves. To account for this, the Cagniard path can be extended by a loop around the smallest branchpoint $1/c_p$ as indicated in Fig. 4(b). We find the following expressions for Green's function $G^s(x,z,t)$

$$\{G_x^s(x,z,t),G_z^s(x,z,t)\} = \begin{cases} 0 & \text{for} \quad -\infty<t<t_{hw}, \\ \frac{1}{\pi}\mathrm{Im}\left[\{C_x,C_z\}\frac{T_s}{\partial\tau/\partial p}\right]_{p=p_{hw}(\tau)} & \text{for} \quad t_{hw}<t<t_s, \\ \frac{1}{\pi}\mathrm{Im}\left[\{C_x,C_z\}\frac{T_s}{\partial\tau/\partial p}\right]_{p=p_s(\tau)} & \text{for} \quad t_s<t<\infty, \end{cases}$$

where

$$\partial\tau/\partial p = x-\frac{p}{\gamma_s}z+\frac{p}{\gamma_f}z_s, \quad (15)$$

t_s is the travel time of the S-wave, and

$$t_{hw}=\frac{x}{c_p}+\sqrt{\frac{1}{c_s^2}-\frac{1}{c_p^2}}z-\sqrt{\frac{1}{c_f^2}-\frac{1}{c_p^2}}z_s, \quad (16)$$

is the travel time of the head wave.

It should be noted that, for the studied case, two head waves are generated: a PS-head wave related to the P-wavefront in the solid and another one related to the pressure wave in the fluid (see Fig. 1). The Cagniard–de Hoop method does not make a distinction between these two events. Since $c_p>c_f$, the head wave denoted in the derived response is the one associated with the P-wave in the solid.

In the synthetic example, we have shown that the non-geometric PS-wave is observed when the ratio between the dominant wavelength and the source height is fractional ($\lambda/h=1/8$). As explained in the theory, this is caused by the evanescent nature of this wave in the fluid; its amplitude is therefore exponentially dependent on the source height. Figure 5 illustrates the amplitude and phase behaviour of the PS-wave as a function of λ/h, computed with the Cagniard–de Hoop solution for two receiver positions. At the first receiver, located 5 m from the source, the PS-wave is geometric and decays less rapidly than the non-geometric one, visible on the

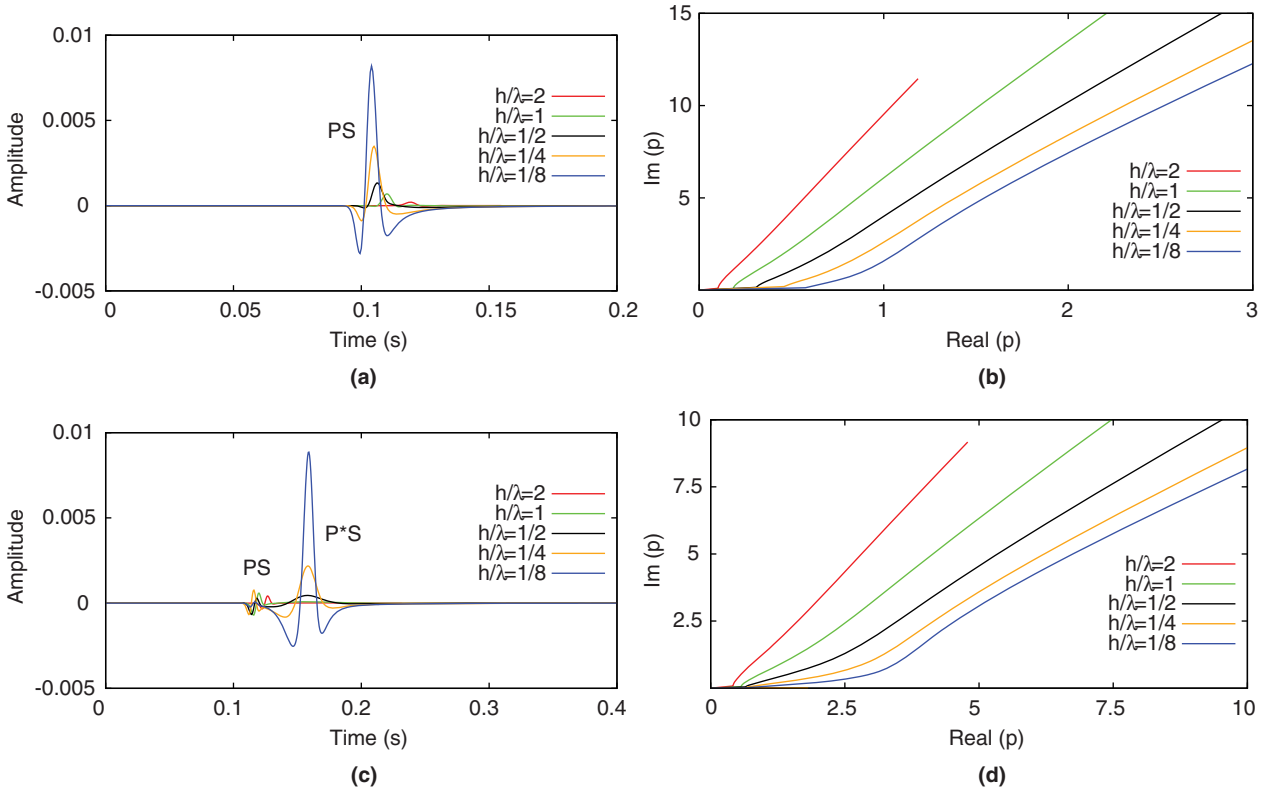

Figure 5 (a) The horizontal component of the PS-wave particle velocity computed using the Cagniard–de Hoop method for different h/λ ratios at a receiver located 5 m away from the source and (b) the corresponding modified Cagniard paths. (c) The PS-wave particle velocity computed for different h/λ ratios at a receiver located 50 m away from the source and (d) the corresponding modified Cagniard paths.

second receiver, as the source is moved away from the interface. The latter even disappears as the ratio λ/h exceeds one. In addition, a clear trend in the associated Cagniard path is observed when the ratio λ/h is increased. For the second receiver, where the non-geometric PS-wave is diverged from the head wave, the curve gets closer to the real axis, and at a certain point, it bends away rapidly. If the source was actually placed on the interface, the contour would intersect with the real axis at this specific point and this ray would correspond to the geometric S-wave arrival (Drijkoningen and Chapman 1988; Hong and Helmberger 1977). The bend in the Cagniard path is due to the ray $p = \sin\theta/c_s$ where θ is the angle shown in Fig. 6. Approximations of non-geometric arrivals can be deduced by expanding around this specific ray (Drijkoningen and Chapman 1988). The range of existence of the non-geometric PS-wave is restricted at one side by $p = 1/c_f$, and therefore, it appears first at the angle $\theta^* = \sin^{-1}(c_s/c_f)$. This implies that the angle of appearance θ^* is dependent on the ratio between the S-wave velocity in the solid and the sound speed in the fluid (c_s/c_f). We can easily verify this by computing the response for the configuration drawn in Fig. 6. The results modelled for two c_s/c_f ratios are displayed in Fig. 7. For a high c_s/c_f ratio of 1000/1500, the non-geometric PS-wave appears at $\theta^* = 41.8°$, where it diverges from the two head waves. However, when c_s/c_f is low, such as 200/1500, the angle of appearance is rather small ($\theta^* = 7.7°$).

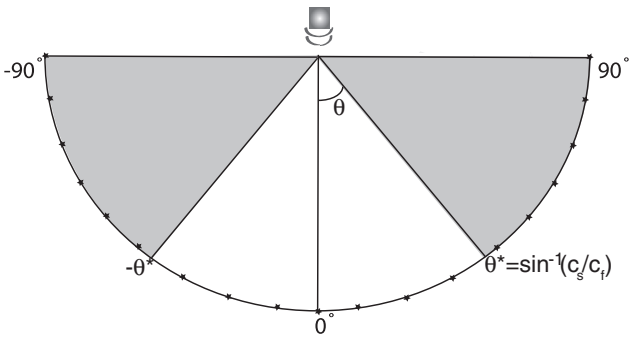

Figure 6 Sketch of the appearance region of the P*S-wave. The grey area indicates the angles at which the P*S-wave appears starting at $\theta*$.

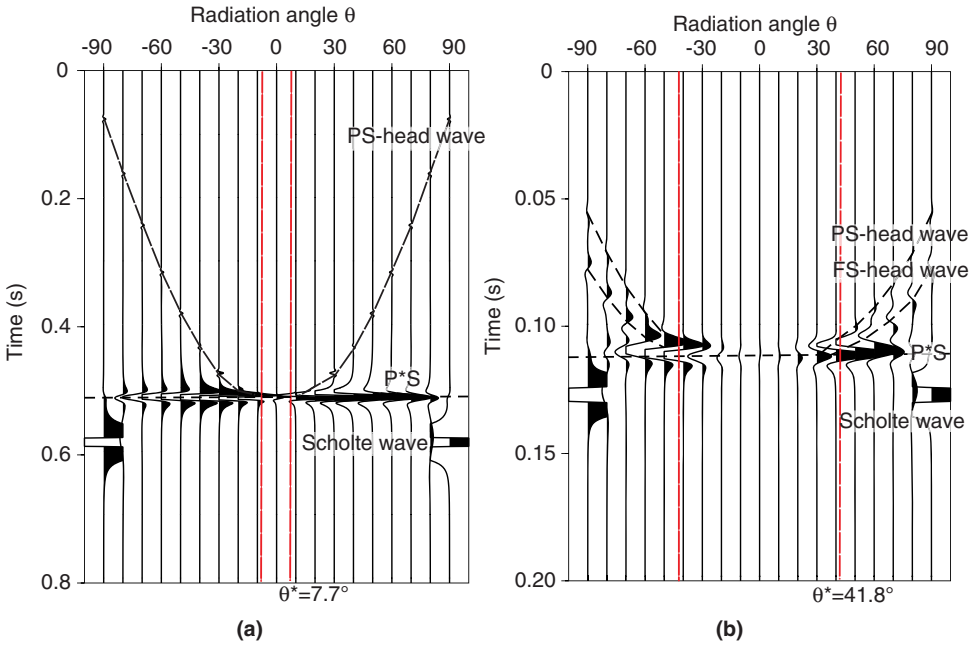

Figure 7 PS-wave particle velocity computed for different angles of incidence with receivers placed in the solid at fixed radius from the source (see Fig. 6 for the configuration): (a) a solid with $c_s/c_f = 200/1500$ and a corresponding angle of appearance $\theta^* = 7.7^\circ$ and (b) a solid with $c_s/c_f = 1000/1500$ and a corresponding angle of appearance $\theta^* = 41.8^\circ$.

4 SEPARATION OF NON-GEOMETRIC PS-WAVES USING LINEAR AND PARABOLIC RADON TRANSFORMS

Based on the discussed properties of the non-geometric PS-wave, it can be stated that this mode has the potential to be useful to infer S-wave information and image the shallow marine subsurface using such S-waves. In particular, the kinematic behaviour of this wave is beneficial. The non-geometric wave behaves as if it was generated at the water bottom without actually having to put the source there. This may considerably increase the efficiency of collecting S-wave data in the field. As shown in the synthetic example, a convenient method to identify these arrivals is to transform the wavefield to the Radon domain. This domain is also appropriate to separate the geometric arrivals from the non-geometric ones as we will show in this section. For this purpose, we define a simple horizontally layered model with the seismic properties shown in Fig. 8 and compute its full response for a source located in the water and receivers on the water bottom using reflectivity modelling (Fuchs and Müller 1971; Schmidt 1988).

In Fig. 9, various types of events are identified and labelled in the computed horizontal component of the wavefield. After performing a linear Radon transform, it can be noticed that the events are quite well separated in this domain. All the P-waves and geometric PS-reflections are mapped within the two lines, representing the horizontal slownesses $-1/c_f$ and $1/c_f$. Outside the denoted region, the non-geometric PS-waves and the Scholte waves are recognized. Practically, we can transform the two regions separately back to the space–time domain, thereby filtering either the geometric or the non-geometric waves. In Fig. 10, the filtered outcomes are compared. In addition to the P-waves and the PS-waves converted at reflectors in the sediments, the apex of the reflection hyperbola, belonging to the PS-modes converted at the water bottom, is confined to the geometric part as well. However, since we aim to process these specific PS-modes, behaving kinematically as pure S-waves, separately, such a filter is not desirable.

To preserve the geometric and non-geometric parts of the PS-waves converted at the water bottom, it is better to filter these in the parabolic Radon domain defined as follows:

$$\check{v}(q, \Gamma) = \int_{-\infty}^{+\infty} v(x, \Gamma + qx^2)dx, \tag{17}$$

where q is the curvature and Γ is the intercept time. Fig. 11 shows the result of transforming the wavefield using equation (17). The appearances of the reflections of interest, denoted by black arrows, are different in this domain. They are identified by their intercept time and their strong curvature.

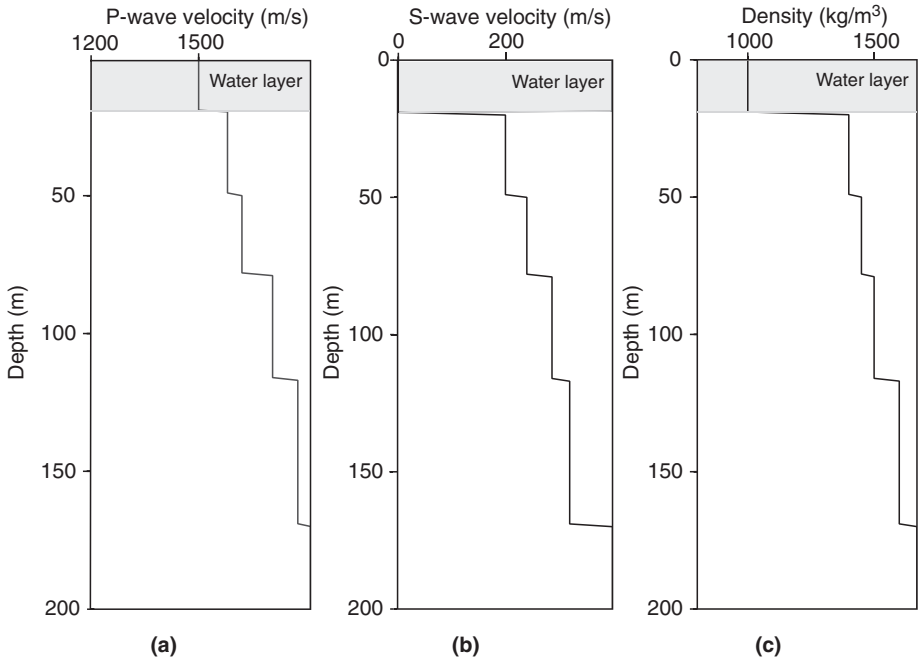

Figure 8 (a) P-wave velocity profile, (b) S-wave velocity profile, and (c) density profile used for the simulations shown in Figs. 8 and 9.

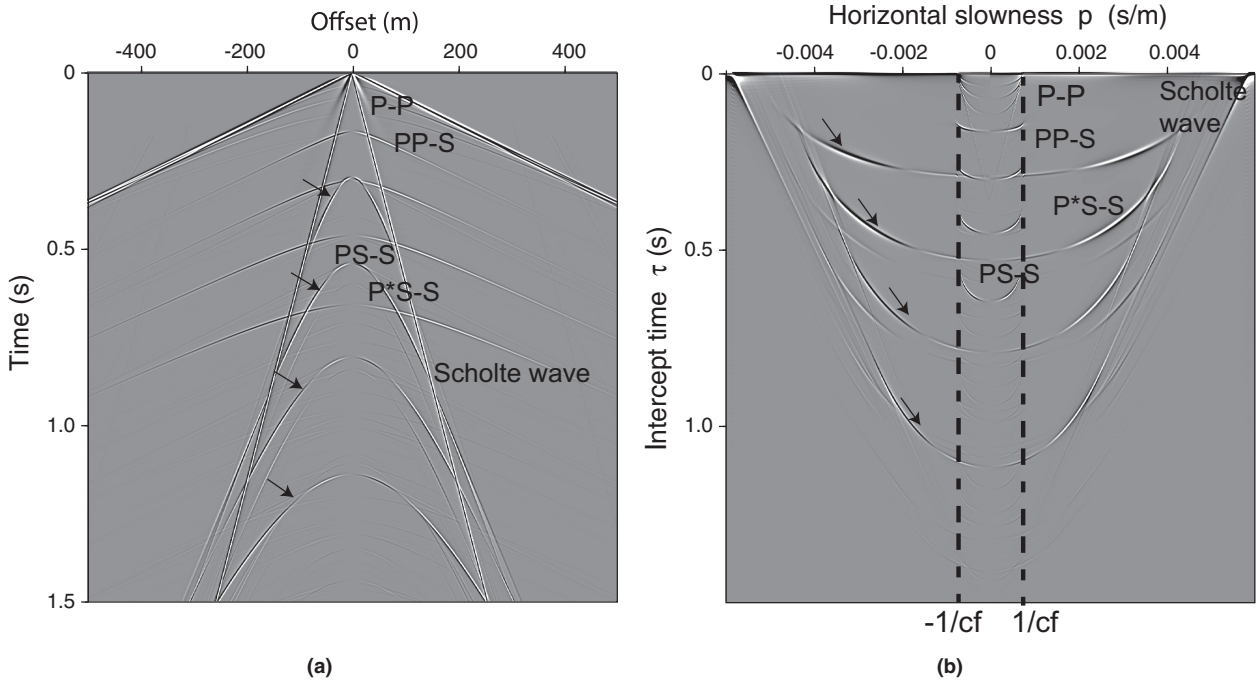

Figure 9 The horizontal component of particle velocity in the space–time domain (a) and in the linear Radon domain (b).

We separate these modes by applying a fan-shaped filter that mutes the reflections with small curvature values. The remaining arrivals are subsequently transformed back to the space–time domain. The final result consists only of modes converted at the water bottom and kinematically behaving as if they were generated by a shear source. These modes can then be processed to obtain an S-wave image of the shallow marine subsurface.

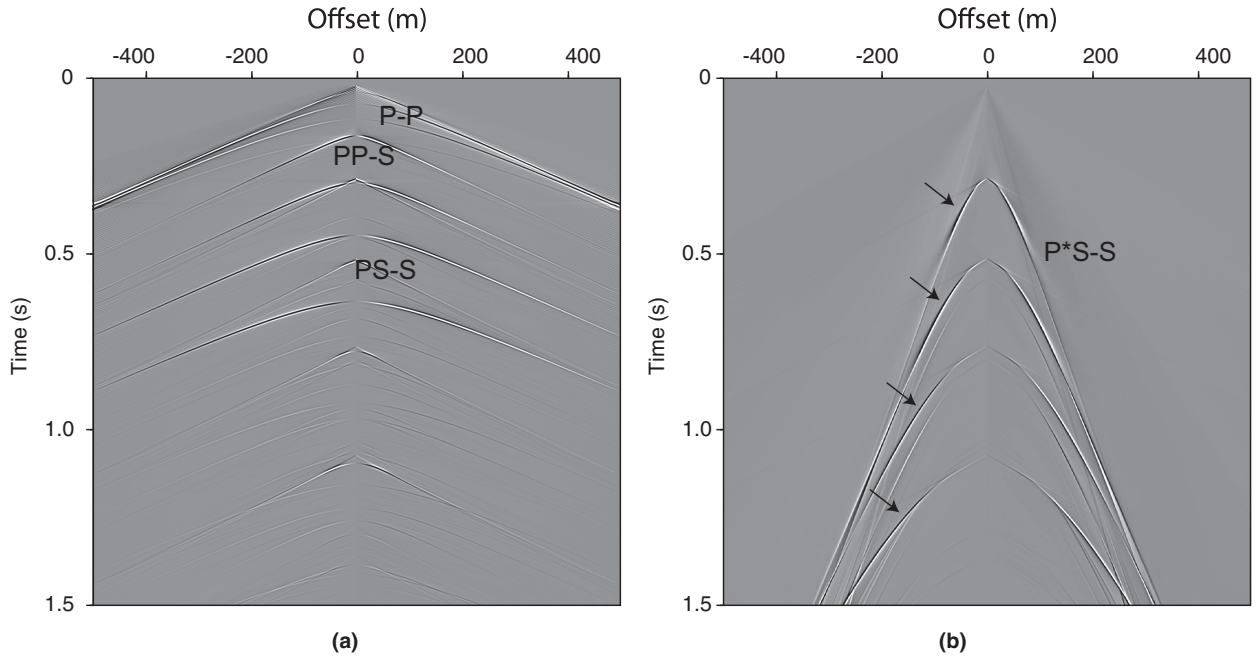

Figure 10 (a) The filtered geometric events and (b) the filtered non-geometric events.

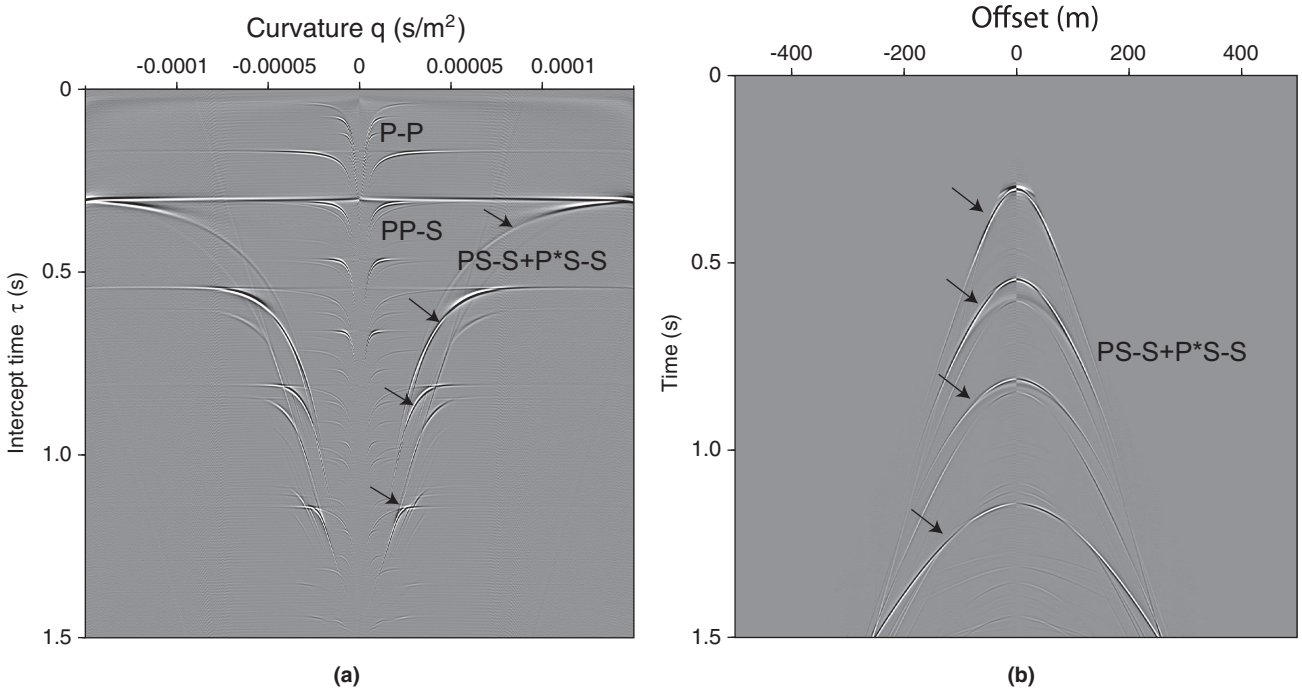

Figure 11 (a) The transformed wavefield in the parabolic Radon domain and (b) the filtered PS-S modes.

5 CONCLUSIONS

The non-geometric PS-wave was observed in shallow marine seismic data. In this paper, we have theoretically explained the existence of the non-geometric PS-wave in a fluid–solid configuration by analysing the transmitted wavefield. This particular mode of conversion is excited only when the S-wave velocity in the solid is lower than the sound speed in the fluid and becomes detectable on synthetic seismograms if the

dominant wavelength of the emitted signal exceeds the source height.

The existence of the non-geometric PS-wave is restricted to a range of horizontal slownesses varying between $1/c_f$ and $1/c_s$, whereas the P-wave is confined to the range 0 and $1/c_p$. In the solid, this wave appears at a specific angle measured from the projection point of the source on the interface, where it diverges from the head waves. This angle of appearance is dependent on the ratio between the S-wave velocity and the sound speed of the fluid. Higher ratios result in lower angle of appearance. This is mainly the case in soft unconsolidated sediments.

The non-geometric behaviour of the P*S is potentially interesting for the seismic method in a shallow marine environment because these specific modes can be treated as pure S-waves generated by a shear source located on the water bottom and their apparent velocity is directly related to the S-wave velocity in the subsurface. Mapping the wavefield in the parabolic Radon domain enables the separation of these waves from the remaining arrivals.

REFERENCES

Aki K. and Richards P.G. 2002. *Quantitative seismology*, 2nd ed. University Science Books.

Allouche N., Drijkoningen G.G., Versteeg W. and Ghose R. 2011. Converted waves in a shallow marine environment: experimental and modeling studies. *Geophysics* **76**(1), T1–T11.

Brekhovskikh L.M. 1960. *Waves in Layered Media*. Academic Press: New York, NY.

Chapman C. 2004. *Fundamentals of Seismic Wave Propagation*. Cambridge University Press.

Daley P.F. and Hron F. 1983. Nongeometric arrivals due to highly concentrated sources adjacent to plane interfaces. *Geophysical Journal International* **73**, 1655–1671.

Daley P.F. and Hron F. 1988. A non-geometrical SH-arrival. *Bulletin of the Seismological Society of America* **36**, 430–445.

de Hoop A.T. and van der Hijden J.H.M.T. 1983. Generation of acoustic waves by impulsive line source in a fluid/solid configuration with a plane boundary. *Journal of the Acoustic Society of America* **74**, 333–342.

Deans D.R. 1983. *The Radon Transform and Some of its Applications*. John Wiley and Sons: New York, NY.

Drijkoningen G.G. and Chapman C.H. 1988. Tunneling rays using the Cagniard-de Hoop method. *Bulletin of the Seismological Society of America* **78**, 898–907.

Fuchs K. and Múller G. 1971. Computation of synthetic seismograms with the reflectivity method and comparison with observations. *Geophysical Journal of the Royal Astronomical Society* **23**, 417–433.

Gutowski P.R., Hron F., Wagner D.E. and Treitel S. 1984. S*. *Bulletin of the Seismological Society of America* **74**, 61–78.

Hong T.L. and Helmberger D.V. 1977. Generalized ray theory for dipping structure. *Bulletin of the Seismological Society of America* **67**, 995–1008.

Hron F. and Mikhailenko B.G. 1980. Discovery of a new nongeometrical S* arrival generated at a free interface. In *Proceedings of the 17th Assembly of the European Seismological Commission*, pp. 293–297.

Hron F. and Mikhailenko B.G. 1981. Numerical modeling of nongeometrical effects by theAlekseev-Mikhailenko method. *Bulletin of the Seismological Society of America* **71**, 1011–1029.

Roth M. and Holliger K. 2000. The non-geometric PS wave in high-resolution seismic data: observations and modelling studies. *Geophysical Journal International* **140**, F5–F11.

Schmidt H. 1988. *SAFARI User's Guide*. SACLANT Undersea Research Centre: La Spezia, Italy.